High-entropy alloy and amorphous alloy composites fabricated by ultrasonic vibrations

Xiong Liang, XiaoLong Zhu, Xin Li, RuoDong Mo, YongJing Liu, Kai Wu and Jiang Ma

---

Articles you may be interested in

High-entropy alloy and amorphous alloy composites fabricated by ultrasonic vibrations

Xiong Liang, XiaoLong Zhu, Xin Li, RuoDong Mo, YongJing Liu, Kai Wu, and Jiang Ma[*]

College of Mechatronics and Control Engineering, Shenzhen University, Shenzhen 518060, China

We successfully fabricate high-entropy alloys and amorphous alloy composites by adopting the proposed ultrasonic vibration method. The low-stress, low-temperature method enables us to create composites that combine both amorphous and crystalline properties. Microscopic observations and computed tomography measurements indicate good bonding quality without pores or cracks in the composites. Due to the unique structure which mixes soft and rigid phases, the composite exhibits improved mechanical performance compared to that obtained from a pure single phase. Our results are promising for the manual design and fabrication of smart materials containing multiple phases and compositions.

amorphous alloy, high-entropy alloy, dual phase composite structure, ultrasonic vibration

PACS number(s): 81.05.Kf, 81.05.Zx, 61.43.Dq

1   Introduction

As newly emerging materials, high-entropy alloys (HEAs) have attracted extensive attention because of their unique compositions, microstructures, and properties compared with traditional materials [1-17]. Compared with conventional alloys, some HEAs have considerably better strength-to-weight ratios, corrosion resistance, oxidation resistance, and, in particular, excellent mechanical performance under extreme conditions [3]; another advantage is the higher tensile strength with superior ductility which results from mechanical twinning or fcc-hcp martensitic transformation [4,18,19]. Since the significant interest that developed in the 2010s, HEAs continue to be a focus of research in materials science and engineering because of their desirable potential for various applications. There was also similar situation for amorphous alloys that were discovered in the 1960s [20-31].

Owing to their remarkable engineering properties, amorphous alloys have caused a surge in research over the past few decades. Although several amorphous alloy systems are considered as HEAs [32-34], most HEAs are crystalline alloys [1,3]. Both of these are multi-component materials, each of which have been widely studied; therefore, fabricating composites of HEAs and amorphous alloys is possibly a good choice for preparing superior alloys. However, thus far, no research on such composites has been reported for either the synthesis of or the properties of these composites.

Recently, an ultrasonic-assisted forming method to process amorphous alloys has been proposed [35-37]. Under high-frequency vibrations, amorphous alloys can soften and deform into certain shapes. By using such methods, micro- to macro-structures were fabricated on the surface of amorphous alloys [35] and even shear punching of amorphous alloys was successfully conducted [36]. In this work, composites of HEAs and amorphous alloys were successfully fabricated by adopting the proposed ultrasonic vibration

*Corresponding author (email: majiang@szu.edu.cn)

method. This new method enables us to create composites that combine amorphous and crystalline properties at low stress and low temperatures. Microscopic observations have indicated good bonding quality. Due to the unique structure which mixes soft and rigid phases together, these composites exhibit more balanced mechanical performance than individual, pure single-phase materials.

2   Experimental

2.1   Materials

$Zr_{35}Ti_{30}Cu_{8.25}Be_{26.75}$ (at%) amorphous alloy ribbons and $Al_{80}Li_5Mg_5Zn_5Cu_5$ (at%) high-entropy alloy ribbons were prepared by a conventional melt spinning process in this work. For convenience in experimentation, the ribbons obtained were cut into lengths ranging from 1 to 3 mm and were mixed with a composition of HEA 5% wt. and amorphous alloy 95% wt.

2.2   Characterizations

The intrinsic characteristics of the HEA, amorphous alloy, and their composite were determined using X-ray diffraction (XRD; Rigaku MiniFlex600, Japan) with Cu Kα radiation. The micromorphologies of the molds and punched products were obtained by a scanning electron microscope (SEM; FEI QUANTA FEG 450, USA). The nanoscale mechanical performance was tested using a Hysitron TI 950 nanoindentation testing system (Bruker, Germany) with a Berkovich tip. The value of the loading rate divided by the load was held constant at 0.05 s^{-1} during testing to maintain a constant indentation strain rate. Microhardness levels were measured with an FM-ARS9000 instrument (Japan). The electron diffraction patterns and energy dispersive spectrometry were conducted using a transition electron microscope (TEM; FEI Titan3 Themis G2, USA). A computed tomography (CT, Sanying precision instruments-nano Voxel 3000d, China) system was used to perform three-dimensional visual characterizations of the welded samples. The characteristics and dimensions of the internal defects in the samples were clearly and accurately displayed.

2.3   Experimental setup

A schematic diagram to illustrate the fabrication of the HEA and amorphous alloy composite is shown in Figure 1(a). Specifically, the mixed ribbons were first stacked together by a clamping force and were followed by the high frequency (~20000 Hz) vibrations of the ultrasonic sonotrode which lasted for several seconds. During this process, the amorphous alloy softened and bonded into a bulk mass with the HEA ribbons wrapped inside the amorphous matrix. As a

result, the HEA and amorphous alloy composite was successfully fabricated. Based on this method, the components and contents of the feedstock materials can be tuned according to specific requirements and the structure and properties of the composites can be complex and changeable. Certain alloys can even be designed based on individual requirements.

3   Results and discussion

3.1   HEA and amorphous alloy composite

Utilizing the method discussed above, a composite of HEA and an amorphous alloy was obtained. Figure 1(b) shows the mixture of the ribbons and final bulk composite material with a diameter of ~5 mm and thickness of ~1 mm. It can be seen that the bulk composite consists of an intact sample exhibiting an apparent metallic luster. The sample size can definitely be tuned by adjusting the size of the ribbon holder and experimental parameters.

3.2   Intrinsic structure and micro morphology

To investigate the intrinsic structure of the HEA and amorphous alloy composite, XRD was used. Figure 2(a) compares the XRD patterns of the composite with HEA and amorphous alloy feedstock materials. It is clear that the diffraction pattern of the composite consists of both the broad amorphous phase and sharp HEA peaks. Figure 2(b) presents an overall SEM image of the composite.

3.3   EDS and electron diffraction patterns

An energy dispersive spectrometer was used to analyze the elemental distributions of the fabricated composite. Figure 2(c) shows the elemental distribution of the composite in a microregion that contains both the amorphous alloy and HEA. In the Al-rich region, the chemical composition should be $Al_{80}Li_5Mg_5Zn_5Cu_5$ (HEA) and in the Zr-rich region, the chemical composition should be $Zr_{35}Ti_{30}Cu_{8.25}Be_{26.75}$ (amorphous alloy). To further study the intrinsic structure, the composite was cut by the FIB at the interface and Figure 2(d) shows the SEM image. For the different regions R1, R2, and R3, diffraction patterns were obtained and are presented in Figure 2(e), (f) and (g), respectively. Clearly, the diffraction pattern on the amorphous alloy side is a typical halo, thus indicating that the structure did not change under the high-frequency vibrations. For interface R2, the diffraction pattern exhibits a halo and crystalline diffraction spots. Furthermore, for region R3, the amorphous halo disappears and only HEA diffraction spots remain. These gradual changes in diffraction patterns reflect the phase composition of the fabricated sample, thus indicating that the composite is composed of
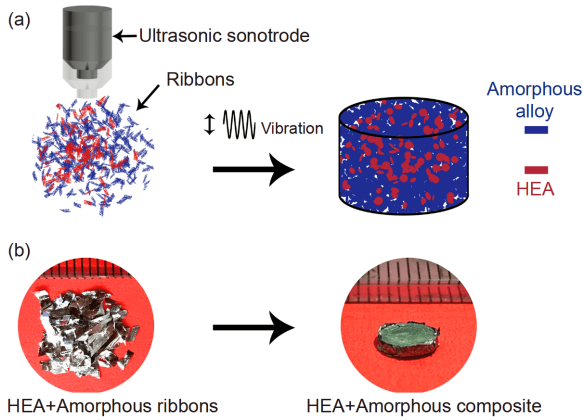
Figure 1 (Color online) (a) A schematic diagram for fabricating the HEA and amorphous alloy composite. (b) A photographic comparison of the HEA and amorphous alloy ribbons and their composite.
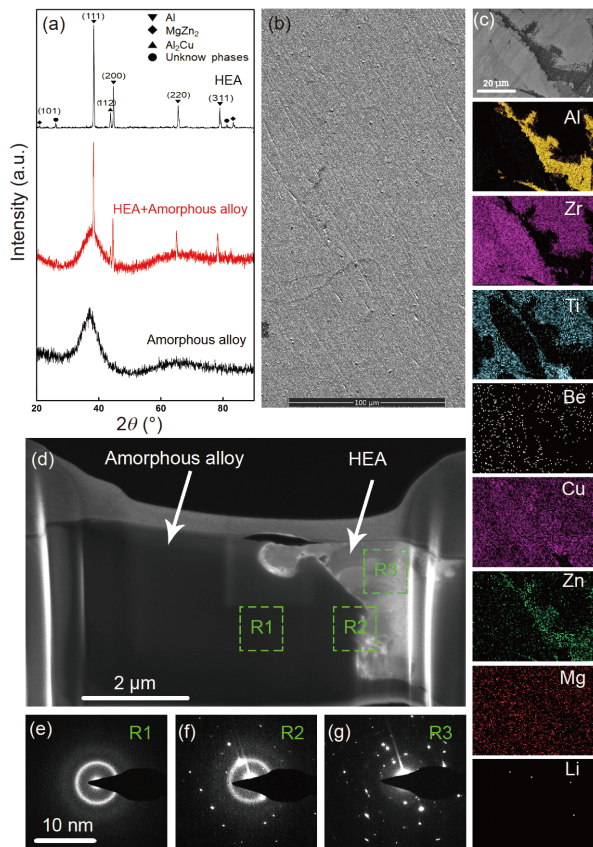
Figure 2 (Color online) (a) The XRD patterns of HEA, amorphous alloy, and their composite. (b) The overall SEM image of the composite. (c) The elemental distributions in a micro-region that contains both the amorphous alloy and HEA. (d) The micro-sectional morphology of the composite fabricated by FIB. The TEM diffraction images of the composite at the corresponding positions of R1 (e), R2 (f), and R3 (g) as shown in (d).

binary distinctive phases.

3.4   Density of the composite

The composite density is an important factor for evaluating

the bonding quality between HEA and amorphous alloys. The density of the fabricated composite was determined to be 5.097 g/cm^3 according to Archimedes' principle. For comparison, the density of the HEA and amorphous alloy ribbons were also examined and their values were 5.167 and 3.054 g/cm^3, respectively. Given these parameters, the calculated density of the composite would be $\rho_{composite}=(w_{amorphous}+w_{HEA})/(w_{amorphous}/\rho_{composite}+w_{HEA}/\rho_{HEA})$. Since $w_{amorphous}$:w_{HEA}=95:5, therefore, the calculated density $\rho_{composite}$=4.994 g/cm^3 is very close to the measured value of 5.097 g/cm^3. The SEM images under different magnification levels also provide solid evidence, as shown in Figure 3. It can be clearly seen that the fabricated sample is dense under magnification levels of 1000×, 2000×, 4000×, and even 8000×, which are shown in Figure 3(a)-(d), respectively.

The observed microtopography indicates that no porosity is present in the composite. Different from the SEM observations, a high-resolution CT system with an actual spatial resolution of 0.5 μm was used to detect defects at a holistic scale. Owing to the use of a high voltage X-ray source with a micro-focal spot and highly sensitive detector, CT can clearly display the inside of the sample and show such features as cracks, holes, and defects. Figure 4(a)-(j) present cross-sectional CT images at different cutting positions from the outer edge to the center. It is evident that the composite is quite dense at the continuous cutting positions and the results indicate that ultrasonic vibrations provide a flexible method for synthetizing the HEA and amorphous alloy composite material.

3.5   Mechanical properties of the composite

The mechanical properties of the composite were also investigated. Figure 5(a) shows the stress-strain curves of the three different materials under compression. The amorphous alloy exhibits the highest fracture strength of 1270 MPa but the poorest plasticity, which is typical for this brittle material. In contrast, HEA has a much lower strength of 664 MPa but exhibits the best plasticity. The composite material inherits the advantages of both initial materials and shows an increased strength of 887 MPa and great improvement in plasticity. It should be noted that only 5% HEA was added in this study. Through minor levels of embedding with HEA, the mechanical performance of the amorphous alloy can clearly be improved. This approach is to address the brittleness of amorphous alloys.

The microhardness of the Zr-based amorphous alloy, HEA, and the composite were also measured and are compared in Figure 5(b). The average Vickers hardness of the amorphous alloys reached 593 HV and the Vickers hardness value of HEA is 190 HV. As a combination of the amorphous alloy and HEA, the composite has an average hardness of 528 HV, which is slightly lower than the hardness of the amorphous
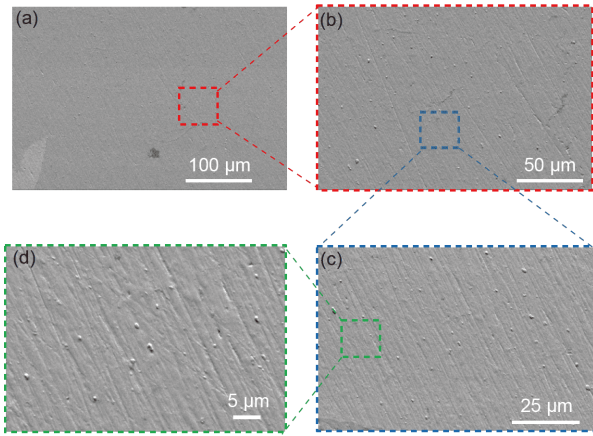
Figure 3 (Color online) SEM images of the fabricated HEA and amorphous composite under different magnification levels. (a) 1000×, (b) 2000×, (c) 4000×, (d) 8000×.
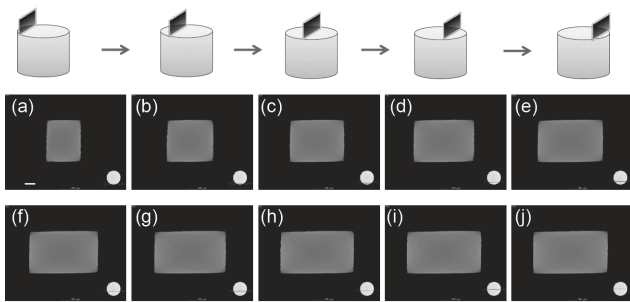
Figure 4 (a)-(j) show the cross-sectional CT images at different cutting positions from the outer edge to the center. The illustration shows how the sample was cut during CT.
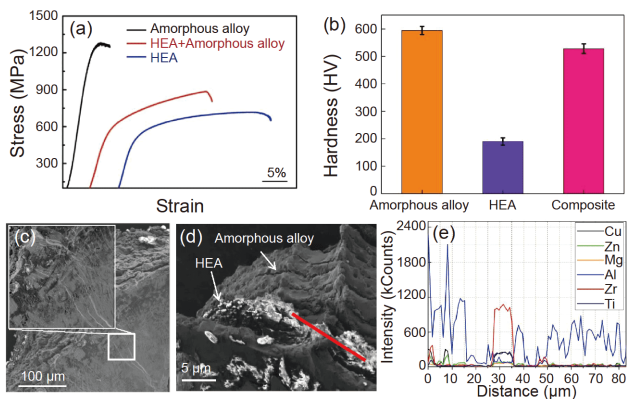
Figure 5 (Color online) (a) Stress-strain curves of HEA, amorphous alloy, and composite when placed under compression. (b) The microhardness of the Zr-based amorphous alloy, HEA, and the composite. (c) The fractographic SEM images of the composite which show the shear bands formed in the amorphous alloy matrix. (d) The SEM image of the fracture morphology after compression. (e) The EDS line scan along the red line in (d).

matrix but is far harder than the HEA.

The fracture morphology of the composite is also investigated to find an explanation for the plasticity enhance-

ment of this material with only a minor addition of HEA. Figure 5(c) shows the fractographic SEM image of the composite and shows the shear bands that formed in the amorphous alloy matrix during deformation. Figure 5(d) shows the SEM image of the fracture morphology after compression. Because of the image contrast, the HEA and amorphous alloy display different brightness in their micromorphology. In this figure, it is evident that HEA particles are strongly sandwiched in the amorphous alloy matrix and even the fractures did not tear them apart, thus indicating the firm bonding present. The EDS line scan along the red line in Figure 5(d) is shown in Figure 5(e) and the elemental distributions are also evidence that the two phases interconnect with each other. The line starts from the HEA particles, where Al is rich and Zr is poor. When the scan reaches the amorphous alloy matrix, the Zr content increases sharply and, after crossing this region, the Zr levels decrease again.

3.6 Mechanisms

Because of the sandwich-like structure, the composite can be considered to be a combination of a rigid phase (amorphous alloy) and soft phase (HEA). The mechanical improvement can be viewed as the result of the interaction between the two distinct phases under stress. During the deformation process, the dislocation accumulates first in the HEA phase with the increase in stress and dominates the plasticity of the composite. The dislocations pile-up to the grain boundaries and transform into an amorphous matrix, which leads to the formation of shear bands with increasing stress, as can be seen in Figure 5(c). The rigid amorphous phase stops the movement of the dislocations and therefore strengthens the mechanical performance of the HEA phase in the composite and shows greater strength than pure HEA. If the material is in the pure amorphous phase, the shear bands would pass through the sample and cause cracking in the amorphous alloy. However, in the composite material, the extension of the shear bands is stopped by the HEA phase; therefore, we can obtain much more favorable plasticity than is provided by the pure amorphous alloy. Figure 6 illustrates the interactions of the soft and rigid phases.
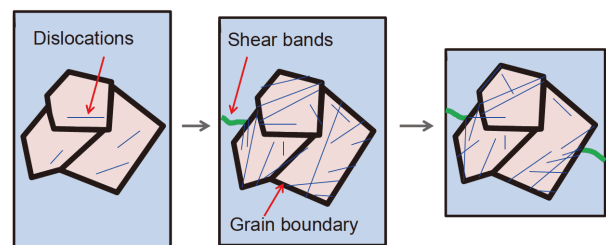
Figure 6 (Color online) A schematic diagram of the soft and rigid phases and their interactions.

4   Conclusions

In summary, by adopting the proposed ultrasonic vibration method, we can fabricate an HEA and amorphous alloy composite. The low-stress, low-temperature method enables us to obtain such a composite with combined amorphous and crystalline properties. Microscope observations and CT measurements show good bonding quality without pores or cracks in the composite. Due to the unique structure that mixes both soft and rigid phases, the composite exhibits improved mechanical performance compared with the pure single phase. Our results can shed light on the manual design and fabrication of smart materials containing multiple phases and compositions.

1   J. W. Yeh, S. K. Chen, S. J. Lin, J. Y. Gan, T. S. Chin, T. T. Shun, C. H. Tsau, and S. Y. Chang, Adv. Eng. Mater. **6**, 299 (2004).
2   B. Cantor, I. T. H. Chang, P. Knight, and A. J. B. Vincent, Mater. Sci. Eng.-A **375-377**, 213 (2004).
3   Y. Zhang, T. T. Zuo, Z. Tang, M. C. Gao, K. A. Dahmen, P. K. Liaw, and Z. P. Lu, Prog. Mater. Sci. **61**, 1 (2014).
4   B. Gludovatz, A. Hohenwarter, D. Catoor, E. H. Chang, E. P. George, and R. O. Ritchie, Science **345**, 1153 (2014).
5   O. N. Senkov, G. B. Wilks, J. M. Scott, and D. B. Miracle, Intermetallics **19**, 698 (2011).
6   F. Otto, A. Dlouhý, C. Somsen, H. Bei, G. Eggeler, and E. P. George, Acta Mater. **61**, 5743 (2013).
7   D. B. Miracle, and O. N. Senkov, Acta Mater. **122**, 448 (2017).
8   S. Guo, and C. T. Liu, Prog. Nat. Sci.-Mater. Int. **21**, 433 (2011).
9   Z. Li, K. G. Pradeep, Y. Deng, D. Raabe, and C. C. Tasan, Nature **534**, 227 (2016).
10   C. J. Tong, M. R. Chen, J. W. Yeh, S. J. Lin, S. K. Chen, T. T. Shun, and S. Y. Chang, Metall. Mat. Trans. A **36**, 1263 (2005).
11   S. Guo, C. Ng, J. Lu, and C. T. Liu, J. Appl. Phys. **109**, 103505 (2011).
12   S. Singh, N. Wanderka, B. S. Murty, U. Glatzel, and J. Banhart, Acta Mater. **59**, 182 (2011).
13   F. Otto, Y. Yang, H. Bei, and E. P. George, Acta Mater. **61**, 2628 (2013).
14   M. H. Chuang, M. H. Tsai, W. R. Wang, S. J. Lin, and J. W. Yeh, Acta Mater. **59**, 6308 (2011).
15   X. H. Yan, J. Ma, and Y. Zhang, Sci. China-Phys. Mech. Astron. **62**, 996111 (2019).
16   C. Meng, J. N. Hao, K. Xu, L. F. Wang, X. L. Shu, S. Jin, and G. H. Lu, Sci. China-Phys. Mech. Astron. **62**, 017111 (2019).
17   H. K. Song, K. Xia, and J. Xiao, Sci. China-Phys. Mech. Astron. **61**, 107011 (2018).
18   D. Wei, X. Li, J. Jiang, W. Heng, Y. Koizumi, W. M. Choi, B. J. Lee, H. S. Kim, H. Kato, and A. Chiba, Scripta Mater. **165**, 39 (2019).
19   D. Wei, X. Li, S. Schönecker, J. Jiang, W. M. Choi, B. J. Lee, H. S. Kim, A. Chiba, and H. Kato, Acta Mater. **181**, 318 (2019).
20   W. Klement, R. H. Willens, and P. Duwez, Nature **187**, 869 (1960).
21   M. Telford, Mater. Today **7**, 36 (2004).
22   W. H. Wang, C. Dong, and C. H. Shek, Mater. Sci. Eng.-R-Rep. **44**, 45 (2004).
23   A. Peker, and W. L. Johnson, Appl. Phys. Lett. **63**, 2342 (1993).
24   C. Schuh, T. Hufnagel, and U. Ramamurty, Acta Mater. **55**, 4067 (2007).
25   T. Nieh, J. Wadsworth, C. Liu, T. Ohkubo, and Y. Hirotsu, Acta Mater. **49**, 2887 (2001).
26   Z. P. Lu, and C. T. Liu, Acta Mater. **50**, 3501 (2002).
27   A. Inoue, Acta Mater. **48**, 279 (2000).
28   P. Gong, X. Wang, Y. Shao, N. Chen, and K. F. Yao, Sci. China-Phys. Mech. Astron. **56**, 2090 (2013).
29   J. F. Li, J. Q. Wang, X. F. Liu, K. Zhao, B. Zhang, H. Y. Bai, M. X. Pan, and W. H. Wang, Sci. China-Phys. Mech. Astron. **53**, 409 (2010).
30   L. S. Chen, J. Z. Zhang, L. Wen, P. Yu, and L. Xia, Sci. China-Phys. Mech. Astron. **61**, 056121 (2018).
31   P. B. Chen, A. D. Wang, C. L. Zhao, A. N. He, G. Wang, C. T. Chang, X. M. Wang, and C. T. Liu, Sci. China-Phys. Mech. Astron. **60**, 106111 (2017).
32   X. Q. Gao, K. Zhao, H. B. Ke, D. W. Ding, W. H. Wang, and H. Y. Bai, J. Non-Crystal. Solids **357**, 3557 (2011).
33   H. Y. Ding, and K. F. Yao, J. Non-Crystal. Solids **364**, 9 (2013).
34   A. Takeuchi, N. Chen, T. Wada, Y. Yokoyama, H. Kato, A. Inoue, and J. W. Yeh, Intermetallics **19**, 1546 (2011).
35   J. Ma, X. Liang, X. Wu, Z. Liu, and F. Gong, Sci. Rep. **5**, 17844 (2015).
36   F. Luo, F. Sun, K. Li, F. Gong, X. Liang, X. Wu, and J. Ma, Mater. Res. Lett. **6**, 545 (2018).
37   J. Ma, C. Yang, X. Liu, B. Shang, Q. He, F. Li, T. Wang, D. Wei, X. Liang, X. Wu, Y. Wang, F. Gong, P. Guan, W. Wang, and Y. Yang, Sci. Adv. **5**, eaax7256 (2019).